Design, Fabrication, and Actuation of Micro-Electro-Mechanical System-Based Image Stabilizer

2010 Jpn. J. Appl. Phys. 49 014201

(http://iopscience.iop.org/1347-4065/49/1R/014201)

Design, Fabrication, and Actuation of Micro-Electro-Mechanical System-Based Image Stabilizer

Jin-Chern Chiou[1,2], Chen-Chun Hung[1*], Chun-Ying Lin[1], and Yung-Jiun Lin[1]

[1]*Department of Electrical and Control Engineering, National Chiao Tung University, Hsinchu 300, Taiwan, R.O.C.*
[2]*School of Medicine, China Medical University, Taichung, Taiwan, R.O.C.*

Received July 2, 2009; accepted September 20, 2009; published online January 20, 2010

In this investigation, we present a two dimensional high aspect ratio *XY* stage, designed as an image stabilizer. This stabilizer is 8 × 8 × 0.75 mm^3, and sufficiently strong to support a suspended image sensor for anti-shaking photographic function. This stabilizer is fabricated by the silicon-on-glass (SOG) process including inductively coupled plasma reactive ion etching (ICP-RIE) processes, in which the anchor layer, pre-etching layer and structure layers are identified without an additional release step as is required in traditional silicon-on-insulator (SOI) wafer etching process. When an actuator is fabricated, flip-chip bonding is adopted to attach a 3 megapixel image sensor to this device. The longest calculated traveling distance of the stabilizer is 25 μm and special stoppers are designed to prevent the actuator from moving out of range, and sticking to the side by pull-in phenomenon. Accordingly, the applied voltage at the 25 μm moving distance is 84 V. Furthermore, the dynamic resonant frequency of the actuating device with an image sensor is 1.013 kHz.

DOI: 10.1143/JJAP.49.014201

1. Introduction

As the photographic cell phone in all instances is gaining popularity all over the world, new digital single lens reflex (DSLR) photography functions for mobile phones are being developed. Anti-shake technology is one of the most important new technologies. Since the number of pixels in a camera has been continuously increasing, undesirable image blurring, caused by hand shake is becoming increasingly serious. The image stabilization function is one of the most popular solutions to this problem.[1)] The familiar elements of image stabilization are lens shifting,[2)] charge-coupled device (CCD) shifting,[3)] and signal processing[4)] among others. Up to now, the most common anti shaking technique used in mobile phones has been signal processing. It requires no additional hardware and does not disrupt the miniaturization of the system module. However, its performance depends strongly on the algorithm used. Because of the need for miniaturization, the lens shifting anti-shaking approach is not suitable, since adding a movable lens causes nonlinearity in control that needs to be compensated for using a complex control algorithm. Image sensor shifting also requires an actuating system associated with the image sensor, but is less disrupting of miniaturization and enable better slimming of the system than the lens shifting method.[1)] In this investigation, a micro-electro-mechanical system (MEMS)-based two dimensional (2D) decoupling actuator is designed to act as an image stabilizer.

MEMS enable suspended microstructures to be precisely moved and integrated with microelectronic circuits monolithically on a chip.[5)] Various actuation mechanisms, such as thermal/bimetallic bimorph.[5–7)] electromagnetic,[8,9)] piezoelectric,[10,11)] and electrostatic actuations,[12,13)] have been proposed and adopted in MEMS-based devices in which mechanical actuation is required.[14)] To summarize all of the driving functions applied in MEMS-based devices, the electrostatic actuator has numerous advantages, such as low power consumption, ease of control, and suitability for use as an image stabilizer designed for a cell phone.

The design of an image stabilizer that is suitable for a cell phone with a 3 megapixel camera requires an actuator that can move by at least 25 μm,[1)] with a sufficiently strong structure to bear the load of a 8 × 8 × 0.75 mm^3 image sensor, from which it must be decoupled two dimensionally when driven. Accordingly, a structure with a high aspect ratio and 150-μm-thick silicon springs and comb fingers is designed. In the decoupled design with an SYMDC micro gyroscope,[2)] movable springs are designed as the decoupling structures. Since the limit of displacement is set to 25 μm, stoppers are designed to prevent the pull-in effect. To achieve design specifications, this device is fabricated using a special silicon-on-glass (SOG) process.[3)]

In this investigation, we propose a two-dimensional decoupling comb-driving actuator, which is manufactured by a special SOG process. This actuator is designed as an image stabilizer that bears the weight of a 6.36 × 6.24 mm^2 image sensor with 3 megapixels.

2. Design

2.1 Principles of operation of electrostatic comb-drive actuator

The *XY* stage designed herein is driven by an electrostatic force.[15)] Figure 1 shows a simple schematic diagram of the comb-driven model. When a potential difference is applied between fixed and movable comb fingers, an electrostatic force is generated, causing the relative displacement of the movable comb fingers (Fig. 1). The driving force F; can be expressed as

$$F = \frac{\partial U}{\partial d} = \frac{1}{2}\frac{nt\varepsilon_0\varepsilon_r V^2}{d}, \quad (1)$$

where U is the energy associated with the applied electric potential V, d is the gap between the fixed and movable comb fingers, t is the thickness of the electrodes, n is the number of pairs of comb fingers, ε_r is the relative permittivity of the dielectric material between the comb fingers, and ε_0 is the permittivity in air. For simplicity, the *XY* stage is considered to follow Hooke's law. The relationship between displacement and the reaction force F_s in the x-direction can be expressed as

$$F_s = k_{x\text{-system}}x, \quad (2)$$

*E-mail address: hungin.ece92g@nctu.edu.tw

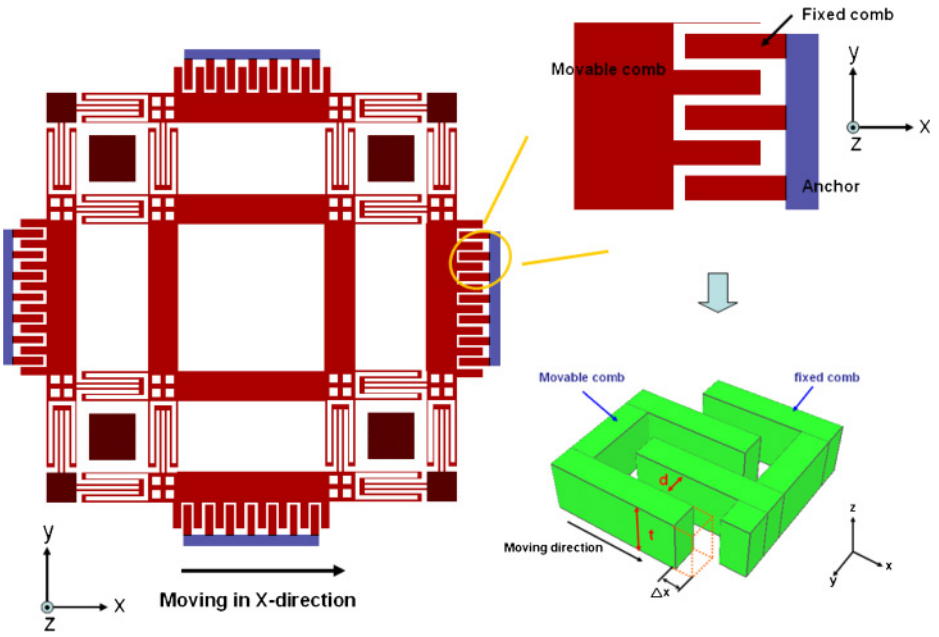

Fig. 1. (Color online) Illustration of comb-finger pair driving principle.

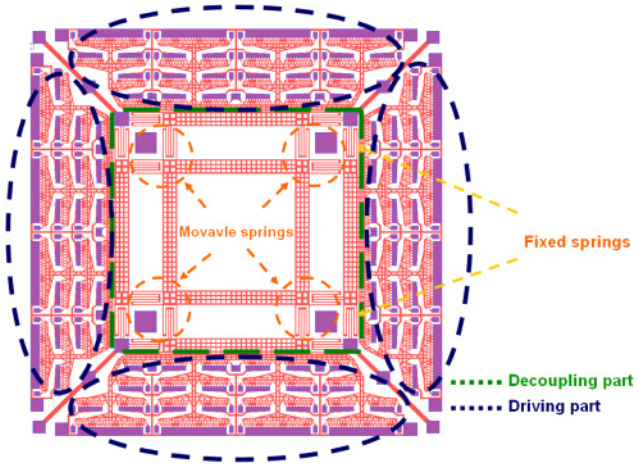

Fig. 2. (Color online) Schematic illustration of decoupling XY stage.

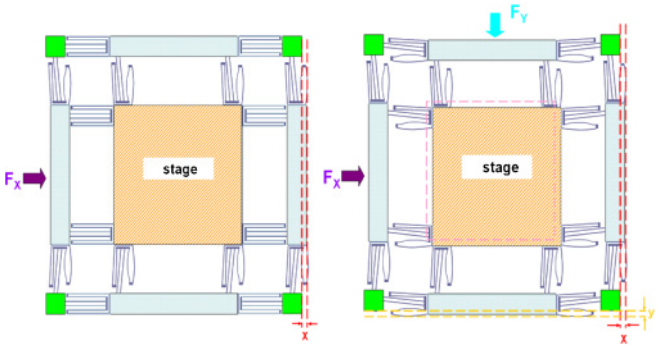

Fig. 3. (Color online) Illustration of driving modes of decoupling XY stage: (a) in only X-direction, and (b) in both X- and Y-directions.

where $k_{x\text{-system}}$ is the equivalent spring stiffness of the system in the X-direction and x is the displacement caused by the electrostatic force. Equation (3) is the sum of eqs. (1) and (2) and specifies the relationship between the displacement x and the driving voltage V:

$$x = \frac{1}{2}\frac{nt\varepsilon_0\varepsilon_r V^2}{dk_{x\text{-system}}}. \tag{3}$$

2.2 Design of decoupling structure

Figure 2 schematically depicts the decoupling XY stage. It includes the decoupling and driving parts of the device. The main decoupling structure is similar to the SYMDC micro gyroscope structure.[16] Given the instability caused by the lateral force, perfect mechanical isolation between the two orthogonal driving directions is important. To achieve this purpose, fixed and movable folded-beam springs are installed in each direction of the XY stage. The driving pair is attached around the decoupling part. Comb-driver finger pairs are chosen as the driving sources to ensure low power consumption and ease of control. When a force is applied in the X-direction only, the XY stage motion and spring flexible situation are as shown in Fig. 3(a). Figure 3(b) shows a simplified mechanism of the operation of the proposed decoupling XY stage when different forces are applied in the X- and Y-directions. On the basic of the assumption that the stiffness of the fixed folded-beam spring is k_{fixed} and the stiffness of the movable folded-beam spring is k_{movable}, the stiffness of the system in the X-direction, $k_{x\text{-system}}$, and that in the Y-direction, $k_{y\text{-system}}$, can be represented respectively; as

$$\begin{aligned} k_{x\text{-system}} &= 2k_{x\text{-fixed}} + 2k_{x\text{-movable}}, \\ k_{y\text{-system}} &= 2k_{y\text{-fixed}} + 2k_{y\text{-movable}}. \end{aligned} \tag{4}$$

In this case, the sizes of the folded beam spring and movable beam springs are equal; thus the stiffness components; $k_{x\text{-system}}$ and $k_{y\text{-system}}$; can be expressed as

$$\begin{aligned} k_{x\text{-system}} &= 4k_{x\text{-fixed}}, \\ k_{y\text{-system}} &= 4k_{y\text{-fixed}}. \end{aligned} \tag{5}$$

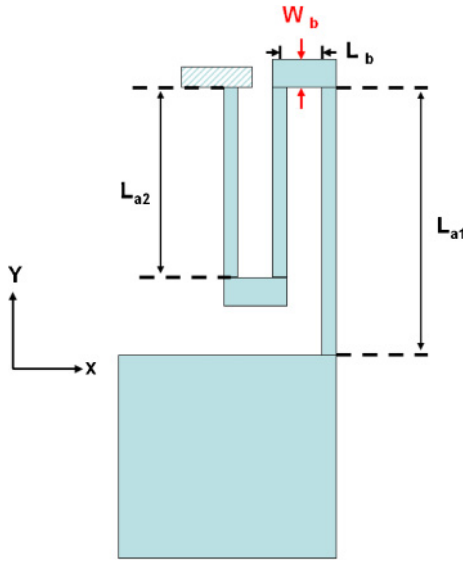

Fig. 4. (Color online) Illustration of folded-flexure spring.

Figure 4 shows the spring design of the structure, based on the energy method.[17] E is Young's modulus, I_a and I_b are the moments of inertia of the different beams, and L_a and L_b are the lengths of the different beams. When the driven force is parallel to the x-direction, the stiffness of a single folded-flexure spring under elastic deformation in the x-direction and the coupled stiffness in the y-direction are calculated as

$$K_{xx} = \frac{48EI_aI_b(3I_bL_{a1} + I_aL_b)}{K_d}, \tag{6}$$

$$K_{xy} = \frac{18EI_aI_b[2I_bL_{a1}(L_{a1} - L_{a2}) - I_aL_bL_{a2}]}{L_bK_d}, \tag{7}$$

where

$$K_d = 3I_a^2L_b^2L_{a2}^2 + 6I_b^2L_{a1}(2L_{a1}^3 + L_{a2}^3) + 2I_aI_bL_b(8L_{a1}^3 + 6L_{a1}^2L_{a2} + 6L_{a1}L_{a2}^2 + L_{a2}^3).$$

In this case, the stiffnesses of all decoupling structures in the x- and y-directions are given by

$$k_{x\text{-system}} = 4k_{x\text{-fixed}} = 4(2K_{xx}) = 8K_{xx} = \frac{384EI_aI_b(3I_bL_{a1} + I_aL_b)}{K_d}, \tag{8}$$

$$k_{y\text{-system}} = 4k_{y\text{-fixed}} = 4(2K_{xy}) = 8K_{xy} = \frac{48EI_aI_b[6I_aL_bL_{a2}^2 + I_b(8L_{a1}^3 - 12L_{a1}^2L_{a2} + 6L_{a1}L_{a2}^2 + L_{a2}^3)]}{L_b^2K_d}, \tag{9}$$

where

$$K_d = 3I_a^2L_b^2L_{a2}^2 + 6I_b^2L_{a1}(2L_{a1}^3 + L_{a2}^3) + 2I_aI_bL_b(8L_{a1}^3 + 6L_{a1}^2L_{a2} + 6L_{a1}L_{a2}^2 + L_{a2}^3).$$

Therefore, when a single direction force is driven parallel to the x-direction, the decoupling ratio of x-displacement to y-displacement in the spring system is defined as

$$\left|\frac{x}{y}\right| = \left|\frac{K_{y\text{-system}}}{K_{x\text{-system}}}\right| = \frac{3[2I_bL_{a1}(L_{a1} - L_{a2}) - I_aL_bL_{a2}]}{4L_b(3I_bL_{a1} + I_aL_b)}. \tag{10}$$

Based on the formula calculations, the decoupling ratio of mechanical stiffness must conform to the system requirement of being larger than 11.1. Table I shows the design specifications of the decoupling XY stage and the image sensor size.

Table I. Specifications of the image stabilizer.

Device size (mm^2)	8 × 8
Image sensor size (mm^2)	6.36 × 6.64
Structure layer thickness (μm)	150
Gap between pair of fingers (μm)	15
Number of comb finger pair	1020
Width of the floded spring (μm)	15
Length of the floded spring L_{a1} (μm)	710
Length of the floded spring L_b (μm)	40
Length of the floded spring L_{a2} (μm)	610
Depth of pre-etching layer (μm)	50

2.3 Design and calculation of range of motion of decoupling XY stage

Most commercial cell phones have a camera with 2 or 3 megapixels but no anti-shaking function. People are always moving and are unable to take a picture without moving at all. Any vibration during taking picture causes blurring. Figure 5 shows the relationship between the number of blurring pixel and the angle of hand shaking. When the camera moves through an angle $d\theta$ in the horizontal plane, the blur pixel number (BP) can be represented as

$$\mathrm{BP} = \frac{d\theta}{\theta_L}P_H, \tag{11}$$

where θ_L is the horizontal angle, and PH denotes the total number of horizontal blur pixels. Typical low-cost camera

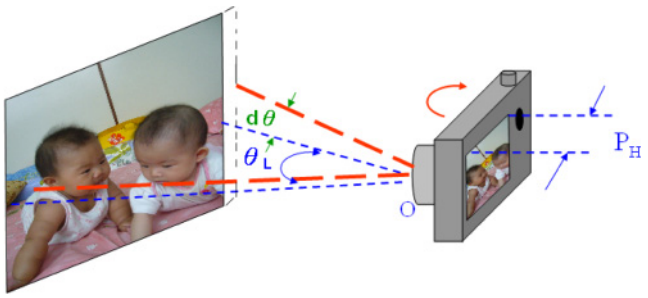

Fig. 5. (Color online) Illustration of relationship between number of blur pixels and hand shake angle.

systems have an angular field of view within 35 to 45°. For a 3 megapixel image sensor with a field of view of 45°, experimental data[18] indicate that a 0.08° horizontal drift occurs in 2 s recording time of hand shaking, as recorded by

an IDG-1000, a dual-axis gyroscope from InvenSense.[19] In this study, an image sensor Micron MT9T012 with 3 megapixels (2056 × 1544 pixels) is employed as the image sensor that is bonded to the designed device. From eq. (11), each pixel corresponds to a horizontal angle of 0.022°. Therefore, the number of horizontal blur pixels is approximately 3.7. Since each pixel of MT9T012 is $2.2 \times 2.2\,\mu m^2$, the *XY* stage must have a range of motion of at least 8.14 µm for adjustment of the blur image. Given that many commercial cameras have ×3 zoom-in and zoom-out functions, the range of motion must be three times this value; or 24.42 µm. In order to achieve the anti-shaking purpose, the moving range in the vertical direction of driven force must be less than 2.2 µm (1 pixel size). This means that the decoupling ratio of *x*-displacement to *y*-displacement should be designed to be larger than 11.1.

3. FEA Modeling Structure

3.1 Static simulation

To elucidate the decoupling effect, stiffness, and natural frequency of the designed *XY* stage, the proposed decoupling actuator is developed using IntelliSuite 8.2. This software is utilized to simulate displacements in plane and the coupled mechanical interference of the *XY* stage in each orthogonal direction. The actual boundary conditions are as follows. 1. The anchors and stators are not displaced because these are in contact with the substrate. 2. The shuttle, rotors, and flexure beams are suspended above the substrate, making the parts free. For simplicity, the shapes of the spring and anchor structures are kept and the other structures are calculated of the mass, being equal to the cube of the same weight as the real device: When simple moldings of the designed moving spring and a frame-loaded spring as the same size as the image stabilizer are fabricated, distinct decoupling occurs, as presented in Figs. 6(a) and 6(b) respectively. In this simulation, a 0.02 MPa pressure in the *X*-direction results in a 1.33 µm displacement in that direction, but only a 0.01 µm displacement in the *Y*-direction. The simulation decoupling ratio of *x*-displacement to *y*-displacement is 133 and shows excellent decoupling effect in the design of movable springs.

To estimate the above stiffness of this designed structure, a simple simulation is performed: a force in a single direction is applied to one side of the *XY* stage. The resulting displacement of the *XY* stage in the static simulation demonstrates that when the force is 1000 µN in both the *X*- and the *Y*-directions, the displacement in the *x*-direction is 4.86 µm and the simulated system stiffness of simulation in the *X*-direction is 205.42 µN/µm, as calculated by using eq. (2).

3.2 Dynamic simulation

To verify the vibration characteristics when the *XY* stage is under dynamic loading, an instantaneous analysis using the finit element method (FEM) software; Intellisuite 8.2; is performed to determine the resonant frequency and modal shape of the designed structure. In this simulation, the weights of the *XY* stage and image sensor are calculated and found to be equivalent to a proof mass shown in Fig. 7. The simulated resonant frequency of the first mode is 1280.1 Hz, that of the second mode is 1280.2 Hz, and that

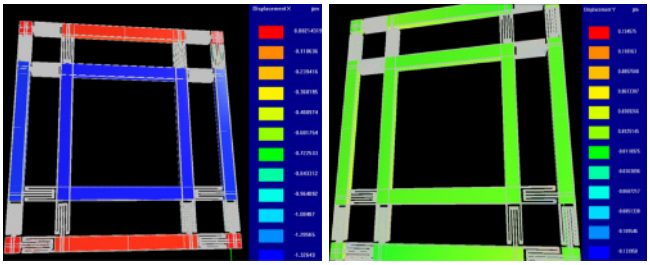

(a) (b)

Fig. 6. (Color online) Decoupling simulation of the *XY* stage in: (a) *X*-direction, and (b) *Y*-direction when driving force in *X*-direction only.

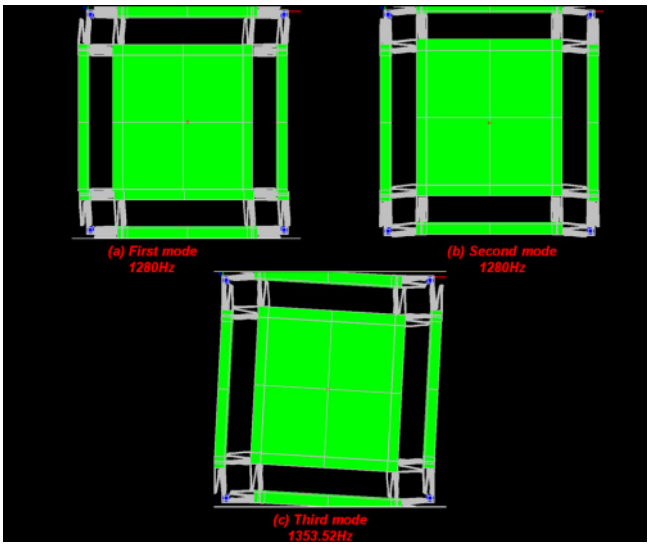

Fig. 7. (Color online) Dynamic modal shapes of *XY*-stage in (a) first mode, (b) second mode, and (c) third mode.

of the third mode is 1353.52 Hz. Since the stabilizer is a symmetrical device, the resonant frequencies of the first and second modes are almost the same but they operate in the *X*- and *Y*-directions, respectively. The third mode involves rotation in the *XY* plane, and its resonant frequency is given by

$$F_{\text{resonant}} = \frac{1}{2\pi}\sqrt{\frac{k}{M}}, \tag{12}$$

where F_{resonant} is the resonant frequency, stiffness of the device structure in *X*- and *Y*-directions $k = 205.42\,\mu N/\mu m$, obtained by simulation, and *M* is the mass of the *XY* stage. These parameters yield a calculated F_{resonant} of 1.248 kHz.

4. Fabrication

4.1 Fabrication of image stabilizer

The decoupling *XY* actuator has an area of $8 \times 8\,mm^2$, exploits anodic bonding, and is produced by double-side alignment photography and inductively coupled plasma reactive ion etching (ICP-RIE). Figure 8 shows the fabrication process, which begins with a 200-µm-thick 100 silicon wafer. In basic RCA cleaning, a thin 8000-Å-thick layer of Al is deposited by DC sputtering [Fig. 8(a)] as the first hard mask for the anchor structure during the second ICP-RIE process [Fig. 8(b)]. Then, the pre-etching layer (for the uniformity of etching rate of ICP process consideration) is

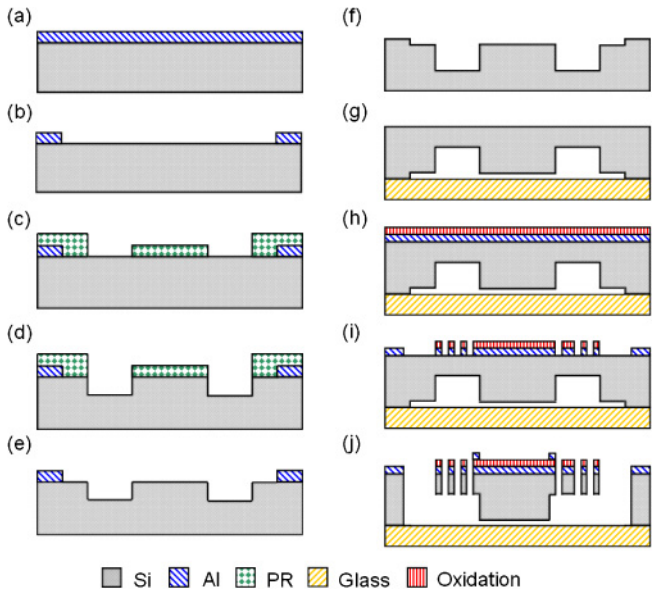

Fig. 8. (Color online) Fabrication process flow of image stabilizer: (a) deposition of first hard mask by Al sputtering, (b) anchor definition by Al etching, (c) pre-etching layer definition by PR coating and lithography, (d) pre-etching layer definition by first ICP-RIE step, (e) anchor definition by second ICP-RIE step, (f) RCA cleaning of Si structure layer, (g) anodic bonding to combine Si structure and glass holder, (h) deposition of Al and oxidation layers as conductive and isolation layers respectively, (i) structure hard mask definition by oxidation and Al wet etching, and (j) the third ICP process to release device structure.

patterned using the photoresister AZ4620 as the second hard mask in the second lithographic process [Fig. 8(b)]. Notably, the pre-etching layer (in the second lithographic process) is required to balance the Si etching rate in the ICP process. Because the etching rate over a large area exceeds that over a smaller area, that at the edges of the Si wafer exceeds that in its center. The design of the pre-etching layer can ensure etching uniformity and prevent the notching effect from happening. The photoresist AZ4620 was removed [Fig. 8(c)] after the first ICP-RIE process to define the pre-etching area with a depth of 50 μm [Fig. 8(d)]. The second ICP process used Al as the hard mask to form the anchor structure with a depth of 100 μm [Figs. 8(e) and 8(f)]. After these processes had been completed and Al had been removed, RCA cleaning was necessary because the Si and glass surface must be very clean. Anodic bonding was then employed to combine the Si wafer with Pyrex 7740 glass [Fig. 8(g)]. An 8000-Å-thick layer of Al was deposited on Si as the conductive layer and a hard mask was used to define the device structures in the third lithographic process [Fig. 8(h)]. A double-sided aligner was used to define layer of the structure before Al was etched and the photoresister was restricted. Then, a 1-μm-thick layer of SiO_2 was deposited as the isolation layer by plasma enhanced chemical vapor deposition (PECVD) [Fig. 8(i)]. The fourth lithographic process was used to pattern the same mask as that the third lithographic process to cover the Al layer completely and prevent shorting between the structure layer and the ball-bond layer that is designed to bond image sensor. Finally, a third Al deposition process and the fifth photolithographic process are applied to define the ball-bond area of the image sensor. Finally, a third ICP-RIE process is utilized to etch

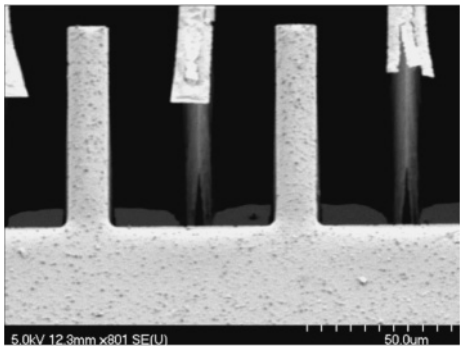

Fig. 9. Phenomenon of overetching in ICP releasing process without compensation design.

Si to a depth of 150 μm until the structure is released [Fig. 8(j)]. Notably, the ICP-RIE parameters had to be controlled very strictly to ensure that all of the device structures were released simultaneously.

4.2 Design of ICP uniformity improvement by mask layout design

The deviation of the etching profile shape is a very important consideration in the design of the proposed device. A change in the shape of the etching profile will significantly affect driving voltage, system stiffness, and loading capability. In ICP-RIE, as the aspect ratio of the etched trench increases, the effective removal of the passivation layer becomes more important, mainly because of ion flux decays toward the bottom of the trench,[19] producing variations in the etching rate between the narrow and the wide etching areas. Since the developed structures are released by the ICP process, the variation in the etching rate results in different releasing times in different areas. Figure 9 shows a plot of the etching results of the ICP releasing process without mask design compensation. Overetching occurs in spacious etching areas when all device structures have been released. To solve this problem, a pre-etching layer and a dummy anchor are designed on the basis of the experimental results and adopted to fill spacious etching areas and ensure that the release process is completed in the entire structure simultaneously. The pre-etching layer in narrow spaces in the device, such as the space between comb fingers, is designed to reduce the etching time in the final releasing process. Dummy anchors are designed to extend the etching time in large etching areas. Figure 10 shows the optical microscopic image and scanning electron microscopy (SEM) images of the device. This indicates that dummy anchors fill the large etching area to balance the release time.

5. Assembly

The flip-chip technique is used to combine an image sensor and an image stabilizer in a wire bonding task. Since the image stabilizer is entirely suspended in midair, bonding the sensor directly to the actuator is very difficult. Suspended springs of the decoupling XY stage may break. To solve this problem, dummy anchors are designed to carry the weight of the device and resist pressure during the flip-chip bonding process and wire bonding processes. Figure 11 shows the design of the dummy anchor and the flip-chip bonding process. A flip-chip bonder is applied to bond the image

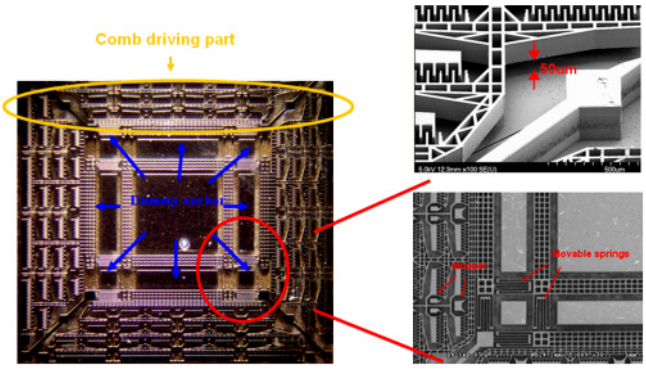

Fig. 10. (Color online) Optical image and SEM images of MEMS-based *XY* decoupling stage.

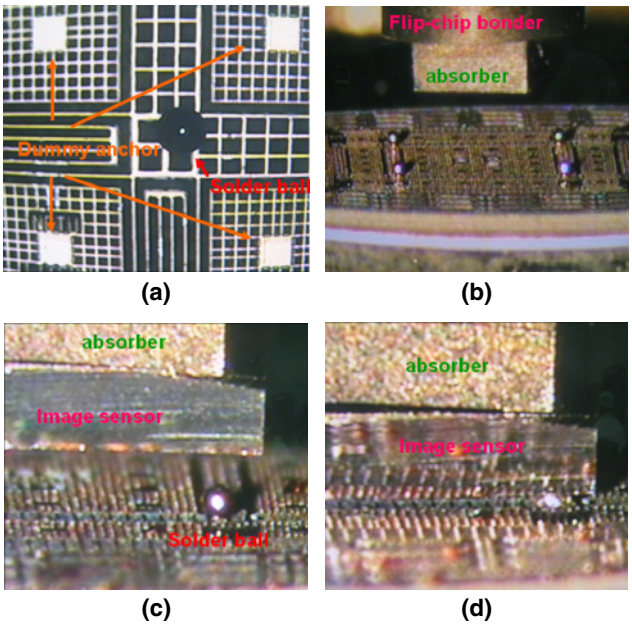

Fig. 11. (Color online) Flip-chip bonding process: (a) locating of solder ball, (b) locating solder ball on *XY* stage, (c) utilizing flip chip bonder to accomplish alignment of image sensor and *XY* stage, and (d) attaching image sensor upon *XY* stage after fusing solder balls.

sensor onto the image stabilizer. Firstly, a 2-μm-thick layer of Al is sputtered onto the back of an image sensor to ensure the adhesion between the solder balls and the image sensor. Then, four solder balls of 100 μm radius are positioned in the bonding area and heated to 236 °C to soften them. The connection positions are designed to form a grid of structure for tracking the solder balls. Finally, the image sensor is pressed onto the solders such that they form contact with the image stabilizer. Since the dummy anchors and image stabilizer are in the same plane before bonding, the dummy anchors support the image sensor and prevent the suspended beam from snapping. Even though a small gap exists between the flattened solder balls during bonding, 150-μm-thick suspended springs are sufficiently strong to tolerate this defect. Figure 12 shows the actuator bonded on an image sensor. Consequently, dummy anchors also support the image sensor during wire bonding. In fact, the design of a dummy anchor not only solves the problem of the breaking of a spring when the sensor is connected to the actuator in

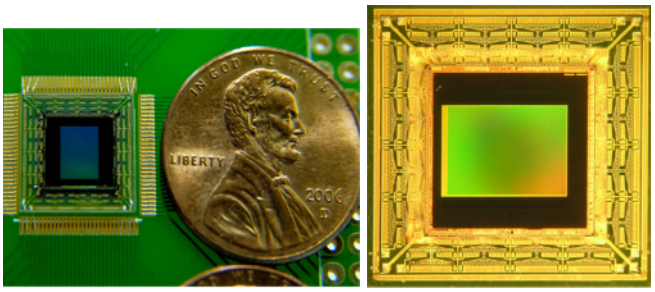

Fig. 12. (Color online) Pictures of *XY* stage bonded to image sensor.

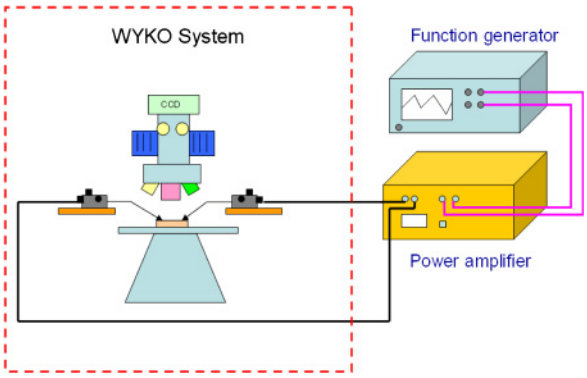

Fig. 13. (Color online) Illustration of static measurement of WYKO system.

the wire bonding process, but also ensures the uniformity of etching in the ICP process.

6. Experimental Results and Discussion

To demonstrate the performance of the fabricated device, a 2D decouple image stabilizer was statically characterized. During the static driving test, the actuator was driven by a DC voltage. The displacement of the actuator was measured by using the WYKO shown in Fig. 13. In the experiments, the displacement was 25 μm when a 84 V driving voltage was applied and with only a 0.2 μm displacement along the vertical axis. The experimental decoupling ratio of *x*-displacement to *y*-displacement is 125 and conforms to the system requirement (larger than 11.1). Figure 14 shows the variation in the displacement with corresponding driving voltage. Notably, when the driving voltage exceeds 84 V, the displacement of the image stabilizer is limited to 25 μm because stoppers prevents pull-in. The difference between the simulation and experimental results in static measurement which is mainly caused by the undercutting of comb fingers during the fabrication process. An undercutting phenomenon of comb fingers causes a larger gap between a pairs of fingers and reduced the electrostatic force when the device is driven at a specific voltage. In dynamic characterization, a MEMS motion analyzer (MMA) system is set up to measure the resonant frequency of this image stabilizer. Figure 15 shows the measurements and the resonance frequency that reached 1.01 kHz. The experimental results were 21.1% lower than the simulated first natural frequency, 1280 Hz. The discrepancy is caused by the inaccuracy of the fabrication process. Further, the simulation model does not

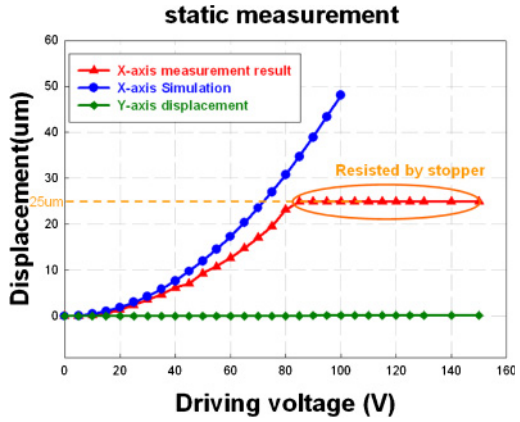

Fig. 14. (Color online) Static measurement of *XY* stage in *X*- and *Y*-directions when driven in *X*-direction only.

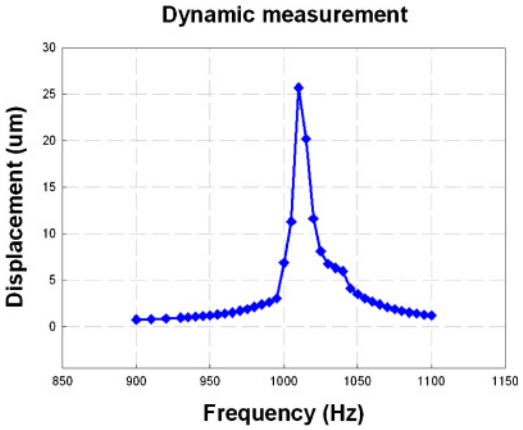

Fig. 15. (Color online) Measurement result of dynamic nature frequency.

take into account the weight of solder balls; this factor may cause some diversity in the purposed desired.

7. Conclusions

An integrated micro-decoupling *XY*-stage is designed, simulated, and fabricated. The integrated *XY*-stage is designed to load a 3 megapixel image sensor fabricated by a through-silicon via technique. It can be applied in commercial cell phone cameras as an anti-shaking system. This proposed device is mainly composed of a silicon-based *XY*-stage, and a comb actuator, which is fabricated by a SOG procedure with three ICP-RIE processes, and the flip-chip bonding technique. Precise calculation of ICP-RIE rate and a favorable pre-etching layer design can increased the yield of the fabrication process. Experimental results indicate that a driving voltage of 84 V can cause a displacement of 25 μm in the driving direction and a displacement of 0.2 μm in the vertical direction, consistent with the anti-shaking purpose. The variation between the simulation and the experimental results is caused by the undercutting of comb fingers resulted during the ICP-RIE process. A stopper effectively prevents the pull-in phenomenon. In dynamic characterization, the natural frequency of the designed *XY*-stage is measured using an MMA system and found to be 1.01 kHz.

Acknowledgements

This work was partially supported by the Lite-On Technology Corporation, and the National Science Counsel under contract Nos. NSC 97-2220-E-009-026, and NSC97-2220-E-009-044-. The authors would also like to thank the Rigidtech Technology Corporation for technical support.

1) D. H. Yeom, N. J. Park, and S. Y. Jung: Int. Conf. Control, Automation and Systems, 2007, p. 2201.
2) K. Sato, S. Ishizuka, A. Nikami, and M. Sato: IEEE Trans. Consum. Electron. **39** (1993) 461.
3) Y. Okamoto and R. Yoshida: Electron. Commun. Jpn., Part III **81** (1998) No. 11, 11.
4) G.-R. Chen, Y.-M. Yeh, S.-J. Wang, and H.-C. Chiang: Proc. 2000 IEEE Asia–Pacific Conf. Circuits and Systems, 2000, p. 101.
5) A. Mohamed, H. Elsimar, and M. Ismail: Proc. Symp. Design, Test, Integration and Packaging of MEMS/MOEMS, 2003, p. 214.
6) D. O. Popa, H. K. Byoung, J. T. Wen, H. E. Stephanou, G. Skidmore, and A. Geisberger: Proc. IEEE Int. Conf. Robotics and Automation, 2003, p. 1470.
7) A. Tuantranont and V. M. Bright: Proc. IEEE Int. Conf. Industrial Technology, 2002, p. 941.
8) G. R. Chen, Y. M. Yeh, S. J. Wang, and H. C. Chiang: Proc. IEEE Asia–Pacific Conf. Circuits and Systems, 2000, p. 101.
9) C. H. Ji, Y. K. Kim, and B. K. Choi: Proc. IEEE/LEOS Optical MEMS, 2000, p. 97.
10) J. Y. Park, Y. J. Yee, H. J. Nam, and J. U. Bu: Proc. IEEE Microwave Symp. Dig., 2001, p. 2111.
11) Y. Haddab, N. Chaillet, and A. Bourjault: Proc. IEEE Int. Conf. Intelligent Robots and Systems (IEEE/RSJ IROS), 2000, p. 659.
12) E. S. Hung and S. D. Senturia: J. Microelectromech. Syst. **8** (1999) 497.
13) X. H. Mu, M. Kahrizi, and L. Landsberger: Proc. IEEE Canadian Conf. Electrical and Computer Engineering (IEEE CCECE), 2003, p. 133.
14) J. C. Chiou and Y. J. Lin: J. Micromech. Microeng. **15** (2005) 1641.
15) W. C. Tang, T.-C. H. Nguyen, and R. T. Howe: Proc. IEEE Micro Electro Mechanical Systems, 1989, p. 53.
16) S. E. Alper and T. Akin: J. Microelectromech. Syst. **14** (2005) 707.
17) Q. Shi, S. Wang, A. Qiu, Y. Xu, and X. Ji: Proc. IEEE Int. Conf. Nano/Micro Engineered and Molecular Systems, 2006, p. 18.
18) D. Sachs, S. Nasiri, and D. Goehl: Image Stabilization Technology Overview [http://www.invensense.com/shared/pdf/ImageStabilizationWhitepaper_051606.pdf].
19) R. Abdolvand and F. Ayazi: Sens. Actuators A **144** (2008) 109.